# CrI₃ revisited with a many-body *ab initio* theoretical approach

Tom Ichibha ⬡,[*] Allison L. Dzubak, Jaron T. Krogel, Valentino R. Cooper, and Fernando A. Reboredo

*Materials Science and Technology Division, Oak Ridge National Laboratory, Oak Ridge, Tennessee 37831, USA*

CrI₃ has recently been shown to exhibit low-dimensional, long-range magnetic ordering from few layers to single layers of CrI₃. The properties of CrI₃ bulk and few-layered systems are uniquely defined by a combination of short-range intralayer and long-range interlayer interactions, including strong correlations, exchange, and spin-orbit coupling. Unfortunately, both the long-range van der Waals interactions, which are driven by dynamic, many-body electronic correlations, and the competing strong intralayer correlations, present a formidable challenge for the local or semilocal mean-field approximations employed in workhorse electronic structure approaches like density-functional theory. In this paper we employ a sophisticated many-body approach that can simultaneously describe long- and short-range correlations. We establish that the fixed-node diffusion Monte Carlo (FNDMC) method reproduces the experimental interlayer separation distance of bulk CrI₃ for the high-temperature monoclinic phase with a reliable prediction of the interlayer binding energy. We subsequently employed the FNDMC results to benchmark the accuracy of several density-functional theory exchange-correlation approximations.

## I. INTRODUCTION

Since graphene was exfoliated, significant advances in experimental techniques have resulted in the rapid discovery of two-dimensional materials [1–5]. These materials provide a broad range of band gaps and electronic properties such as high carrier/thermal conductivity, optochemical reactivity, and piezoresistive effects. Despite this rapid discovery of novel 2D materials, it took nearly a dozen years to discover two-dimensional magnets [6,7].

Recently, it was demonstrated that long-range magnetic order in CrI₃ persists down to a single monolayer [6]. This finding marked a milestone in the community, as the existence of the long-range magnetic order in a two-dimensional material was thought to be prohibited by the Mermin-Wagner theorem. The apparent contradiction was explained by the fact that spin-rotational invariance, a premise in the theorem, is no longer present in CrI₃ because of spin-orbit interactions, which induce single-ion spin anisotropy [8]. An additional interesting finding regarding this material is that the magnetic ordering is intimately related to the stacking configuration and the number of layers. Rhombohedral CrI₃ bulk exhibits ferromagnetic interlayer interactions. On the other hand, few-layered CrI₃ has a different stacking configuration, similar to monoclinic CrI₃ bulk, and exhibits antiferromagnetic interlayer interactions. As a result, monolayer CrI₃ is a ferromagnet, while bilayer CrI₃ is a layerwise antiferromagnet, and trilayer CrI₃ is a layerwise ferrimagnet, in which the layers are magnetized in different directions alternately (denoted as ↑↓↑) [9,10].

This material is particularly attractive owing to the possibility of dynamically controlling the spin orderings in a few-layer CrI₃. For example, an electric or magnetic field applied to bilayer or trilayer CrI₃ switches the spin orderings and consequently alters the magnetoresistance [11–13]. Moreover, bilayer CrI₃ is proposed for use as "the antiferromagnet layer of magnetic tunnel junctions (MTJs)" [11] and "voltage-controlled magnetic memories with low operation energy." [13] A recent work by Song *et al.* [14] reported that the magnetic state can be tuned by pressure. They found that the antiferromagnetic phase of the bilayer CrI₃ vanishes under a pressure of 2.7 GPa. Furthermore, they established that in trilayer CrI₃ a fully ferromagnetic phase ↑↑↑, as well as a new magnetic phase ↑↑↓, appear at high pressures. The ↑↓↑ and ↑↑↓ phases had different numbers of antiferromagnetic interfaces resulting in differences in their respective magnetoresistances. The three magnetic phases remained even after the applied pressure was removed, as such it is thought that a first order structural transitions are involved in the magnetic transitions.

In addition to the experimental research, CrI₃ has been studied theoretically with *ab initio* methods focused on predicting the magnetic ground state and explaining magnetic transitions. For instance, prior to the experimental realization of 2D magnetism in CrI₃ [6], McGuire *et al.* [15] predicted that the ferromagnetic state would be significantly more stable than the nonmagnetic state in monolayer CrI₃ using first principles calculations. Sivadas *et al.* [16] elucidated why the magnetic order of bilayered CrI₃ changes between ferromagnetic and antiferromagnetic depending on the stacking configuration. They explained the magnetic transition by demonstrating that interlayer super-super exchange effects between chromium *d* orbitals mediated by iodine *p* orbitals determine the magnetic state. The configuration-dependent

———————
[*]ichibha@icloud.com

magnetic transition agrees with an experiment showing that trilayer $CrI_3$ has three different magnetic phases with different structures [14].

Nevertheless, accurate predictions with *ab initio* methods for these layered materials remain a difficult problem because of the simultaneous presence of noncovalent interlayer interactions and of highly correlated electrons occupying the $d$ orbitals in Cr, which are both significant challenges for mean field approaches. The introduction of vdW corrections in density-functional theory (DFT) improves the description of the noncovalent interlayer forces, in practice. However, the results are sometimes not quantitatively reliable: They change significantly depending on the parametrization of the van der Waals (vdW) correction and the treatment of the exchange energy [17–20].

To obtain reliable predictions independent of adjustable parameters without the mean-field approximation, we use the fixed-node diffusion Monte Carlo method (FNDMC). This method is one of the most reliable choices since it removes any excited-state components from a wave function using the projection operator, $e^{-\hat{H}\tau}|\Psi\rangle$ ($\tau \to \infty$): The wave function is optimized within the many-body form [21]. FNDMC has made accurate predictions of several layered materials [19,20,22–28]. Mostaani *et al.* [23] calculated the interlayer binding curve of bilayer graphene with FNDMC, successfully reproducing the experimental out-of-plane zone-center optical phonon frequency. Shin *et al.* [22] concluded that bilayer $\alpha$-graphyne is more stable than bilayer graphene using FNDMC, contrary to the DFT prediction. They found that FNDMC predicted a comparatively huge density of electron population between the layers in $\alpha$-graphyne. Thus, they concluded that $\alpha$-graphyne is stabilized by interlayer covalent bond formation in the FNDMC prediction. Kadioglu *et al.* [29] predicted the relative stability of buckled and washboard phases for monolayer and bilayer arsenene.

In this paper, we report FNDMC results on the interlayer binding properties of monoclinic bulk $CrI_3$. We find that FNDMC reproduced the experimental interlayer separation distance [15] without adjustable parameters. In the absence of accurate experimental data for the binding energy, FNDMC provided an accurate benchmark for establishing the accuracy of state-of-the-art approximations used in DFT. We show that the vdW correction in DFT is necessary to reproduce the interlayer binding properties. Most notably, the vdW–DF–optB88 and vdW–DF–optB86b functionals [30] reproduced the FNDMC-reference interlayer separation distance and binding energy.

The rest of the paper is organized as follows: In Sec. II we describe the technical details of our DFT and FNDMC calculations. Especially, we explain how we carefully dealt with the errors peculiar to FNDMC such as the one-body finite-size error, fixed-node approximation error, and time step error. In Sec. III we discuss and analyze our results. We give an accurate prediction of the interlayer binding energy of the monoclinic structure, carefully considering the two-body finite-size error in the bulk and monolayer structures. We show that our FNDMC reproduced the experimental interlayer separation distance. Finally, we evaluate the DFT functionals mentioned earlier compared with the reference binding energy and separation distance. This work is summarized in Sec. IV.
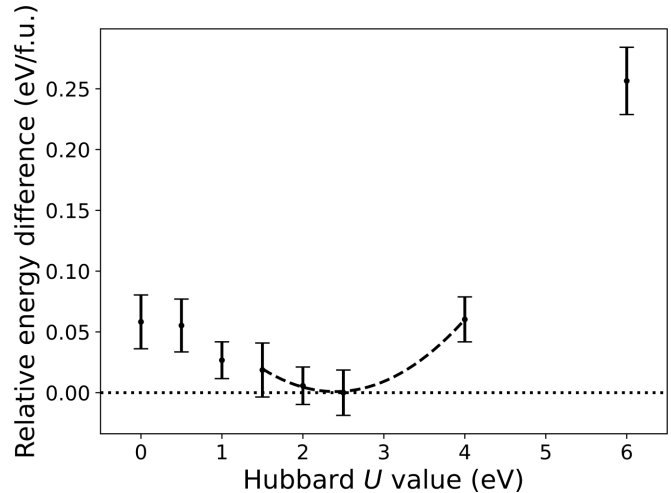


FIG. 1. Total energies of the rhombohedral structure predicted by FNDMC with LDA+$U$ trial wave functions with different $U$ values. The total energies are given as the relative differences from the lowest data point. The optimal $U$ value is estimated to be $U = 2.4(4)\,\text{eV}$ by quadratic fitting (dashed line).

## II. CALCULATION DETAILS

We used QMCPACK [31] for the FNDMC calculations. We used Slater-Jastrow–type trial wave functions [21], which have proved to be sufficiently accurate in numerous applications of FNDMC for both correlated and vdW materials. The orbital functions comprising the Slater determinant were generated by the local-density approximation (LDA) +$U$ method implemented in Quantum Espresso (QE) [32]. We modified the value of $U$ to alter the nodes of the trial wave function. Figure 1 shows the relationship between the FNDMC total energies and the $U$ values. According to the variational principle, optimal nodes correspond to a minimum of the total FNDMC energy. It can be seen that the dependence of the energy on $U$ is weak in this system for low to moderate values of $U$. Since the minimum is estimated to be $U = 2.4(4)\,\text{eV}$ by quadratic fitting, we used $U = 2.5\,\text{eV}$ for all the calculations. We used the BFD pseudopotential for iodine atoms [33,34]. Meanwhile, we used our own pseudopotential for chromium atoms [35], since a 40% decrease in the locality error from the BFD pseudopotentials was achieved with our pseudopotentials for the $3d$ transition metal atoms. Because of the intrinsic plane wave hardness of the potentials, a high-energy cutoff of 300 Ry was required to obtain FNDMC trial wave functions from the DFT calculations [35,36]. The Jastrow factor contained one-, two-, and three-body terms amounting to 160 variational parameters in total, which were optimized by the "linear" method [37] implemented in QMCPACK.

A FNDMC calculation is accompanied by two kinds of system-size errors, which are larger for smaller simulation cells. They are called one- and two-body finite-size errors [38]. The one-body finite-size error is caused by insufficient sampling of the Brillouin zone. This error is suitably handled with twist-averaged boundary conditions that is similar to the $k$-points sampling in DFT. In this paper, we used the reciprocal grid equal to or larger than $3 \times 3 \times 3$ per 2 f.u. The resulting one-body finite-size error was kept below
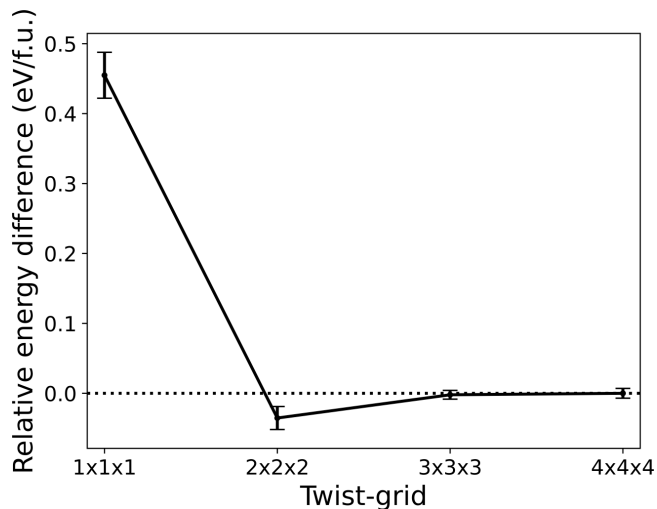
FIG. 2. Total energies per formula unit of the monoclinic structure predicted by FNDMC with different grid sizes of twist-averaging. The total energies are given as relative differences from that with a $4 \times 4 \times 4$ grid. This figure indicates the one-body finite-size error is sufficiently suppressed with a $3 \times 3 \times 3$ grid.

10 meV/f.u., as shown in Fig. 2. The two-body finite-size error is attributed to the overestimation of the interaction distance between an electron and its making exchange-correlation (XC) holes (i.e., a suppression of the electronic density caused by the presence of the electron) in the periodic cells. The influence of periodic images on this interaction is generally negligible for practically used cell sizes [38]. However, in a typical implementation of the potentials under the periodic boundary condition (i.e., Ewald method [39]), an electron is significantly affected by the XC holes of the periodic images. Fortunately, the influence on the total energy can be estimated by extrapolating the total energy on the inverse of the simulation cell size. Also schemes to cancel out the spurious interactions can be used [38]. We used the extrapolation scheme to estimate the two-body finite-size error with the Ewald method as discussed in the first paragraph of Sec. III.

We used the Gaussian charge screening breakup method, an Ewald-class method, rather than the optimized breakup method (default setting of current version of QMCPACK) [40], because of known numerical instabilities in the latter method for some quasi-2D systems [41]. With the Gaussian charge screening breakup method, care must be taken to minimize the error induced by the exclusion of nearest neighbor images in the real-space portion of the Ewald sum. The range of the real-space portion of the Ewald potential is controlled by the LR_DIM_CUTOFF parameter in QMCPACK [31], with a larger cutoff giving a smaller error. We confirmed that cutoffs equaling 15, 20, and 25 gave 136.1, 11.6, and 1.0 meV/f.u. biases, so we used a cutoff equaling 20 or larger.

We set the FNDMC timestep as $dt = 0.005$ a.u.$^{-1}$. We confirmed that the interlayer binding energies calculated with $dt = 0.02$ and $0.005$ a.u.$^{-1}$ were identical within the error bar of one standard deviation ($1\sigma$). We confirmed that the nodal errors and nonlocality pseudopotential errors are small enough to predict the binding properties, comparing the

energy difference of the rhombohedral and monoclinic structures in Appendix A1. We used Nexus [42] for the FNDMC calculations. Nexus is a workflow management system mainly for QMCPACK. Note that the error bars in this work all indicate $1\sigma$ confidence interval.

We also calculated and compared the interlayer binding curves with multiple approximations of DFT implemented in Vienna *ab initio* Simulation Package (VASP) [43] to study how the binding curve depends on the functional. We used the projector-augmented wave (PAW) method to describe the core electrons [44]. We described the Kohn-Sham orbitals by plane waves. The cutoff energy was 520 eV, which is the higher one of the recommended cutoff energies accompanied by the chromium and iodine PAW pseudopotentials. The $k$-mesh spacing was denser than 0.30 Å$^{-1}$, with which the total energy of the monoclinic structure was converged within a few meV per formula unit. For the comparison, we considered the LDA [45], PBE [46], PBEsol [47], and SCAN [48] functionals; vdW interaction corrected vdW–DF [49,50], vdW–DF2 [30,51], vdW–DF–optPBE, vdW–DF–optB88, vdW–DF–optB86b [30], rev–vdW–DF2 [18], and SCAN+rVV10 [52] functionals; and the LDA+$U$ method [53]. Here, VASP implements the vdW-DF-class nonlocal correlation terms with the original formulas [30,49–51], which depends on the electronic density rather than the spin density. On the other hand, there are extended formulas for spin-polarized calculations by Thonhauser *et al.* [54]. We confirmed that the difference of the formulas hardly influences the interlayer binding curve in the supporting information [55].

We used the experimental geometries for the rhombohedral and monoclinic bulk structures, as reported in a previous work by one of the authors (see Table 1 of [15] for details). We targeted the ferromagnetic states for both bulk and monolayer structures (i.e., all the chromium ions magnetized in the same direction). Since all the DFT functionals shown earlier predicted 3 bohr/f.u. magnetization for the bulk and monolayer structures, we used this value for the FNDMC calculations. Although the monoclinic structure is known not to have long-range magnetic order, our DFT calculation with VASP code using the vdW–DF2 functional predicted that the above-mentioned ferromagnetic phase is 1.45 eV/f.u. more stable than the nonmagnetic phase. This indicates that the magnetic moment of the spins are stable but spins may be otherwise disordered (i.e., the materials is likely paramagnetic). We selected the ferromagnetic state as one of the choices of the spin configurations. The energy difference of FM $-$ AFM was only 0.5 meV/f.u..

### III. RESULTS AND DISCUSSION

We calculated the interlayer binding energy of the monoclinic structure. For the interlayer binding energy prediction, care must be taken regarding the two-body finite-size error, since errors are expected to be very different between the bulk and the monolayer. We estimated finite-size errors by extrapolating the total energy for the inverse of the simulation cell sizes. Figure 3 (Fig. 4) shows the total energies for the monolayer (monoclinic bulk) structure calculated with FNDMC as a function of the inverse of the size of the simulation cell. The dotted straight lines shows a linear fit curve using the energies
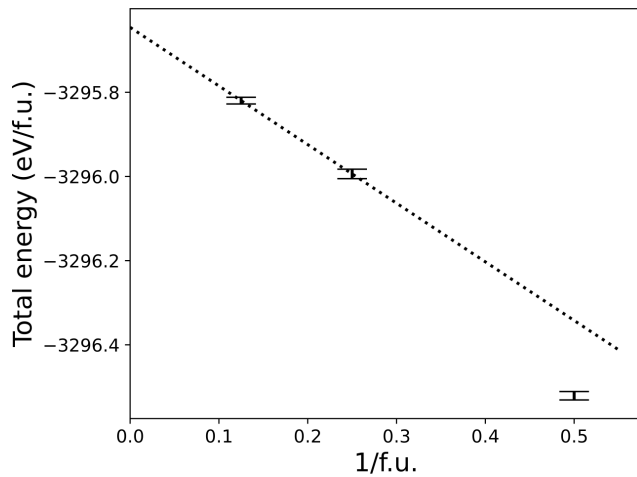
FIG. 3. Total energies of the monolayer $CrI_3$ predicted by FNDMC for the inverse of different simulation cell sizes.

of the larger of the two simulation cell sizes. The y intercept value represents the extrapolated value of the total energy to the infinite simulation cell-size limit. The binding energy is 342 (22) meV/f.u. equaling 16.7(11) meV/$Å^2$.

We calculated the interlayer binding curve of the monoclinic structure with FNDMC to predict the interlayer separation distance. We estimated the two-body finite-size error by a linear extrapolation of the energies of 4 f.u. and 12 f.u simulation cells for the inverse of the cell size. We did not optimize the geometry for every interlayer separation: we merely changed the interlayer separation distance. However, we confirmed that the structural relaxation did not significantly alter the prediction of the separation distance. Figure 5 compares the interlayer binding curves of the monoclinic structure predicted by the vdW–DF–optB86b functional for two different geometries: with and without (fixed) structural relaxation. The vertical lines indicate the minima estimated by cubic spline interpolation, highlighting the minimal effects of structural relaxation on the interlayer separation distance. The binding curve predicted by FNDMC is shown in Fig. 6. The
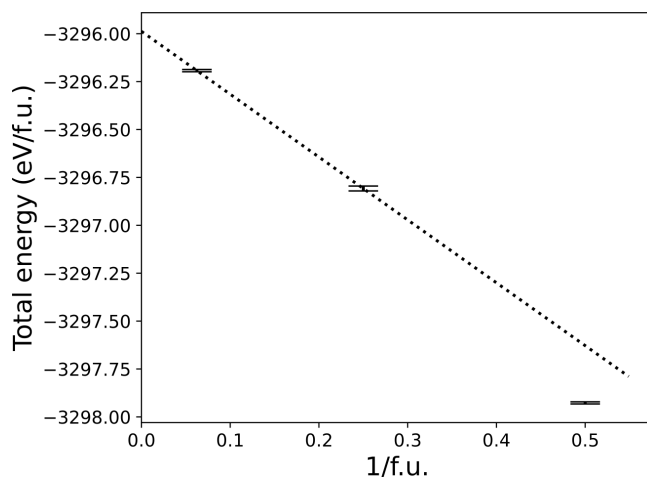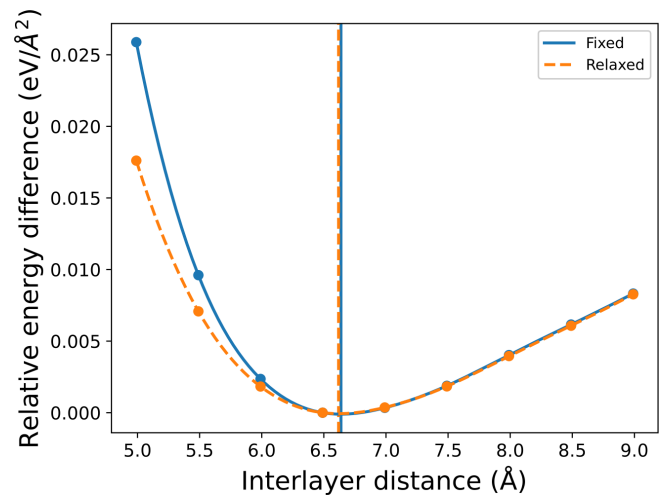


FIG. 5. The interlayer binding curves of the monoclinic structure predicted with vdW–DF–optB86b for two different geometries: experimental and relaxed with vdW–DF–optB86b.

minimum estimated by quadratic fitting is 6.749(73) Å, which agrees with the experimental separation distance 6.623 Å [15] within $2\sigma$ standard deviation. We note that the interlayer separations predicted with 4 and 12 f.u. are 6.496(22) Å and 6.693(26) Å, respectively. The interlayer separation with the 4 f.u. simulation cell is significantly different from the extrapolated value, indicating the need for careful consideration of the two-body finite-size errors when predicting interlayer separation distances.

Figure 7 shows the interlayer binding curves of the monoclinic structure predicted by DFT with different functionals. (The predicted binding curves of the rhombohedral structure are also shown in the Appendix A2. They are very similar to those of the monoclinic structure.) The vertical line indicates the experimental interlayer separation distance [15]. The gray



FIG. 4. Total energies of monoclinic bulk $CrI_3$ predicted by FNDMC for the inverse of different simulation cell sizes.
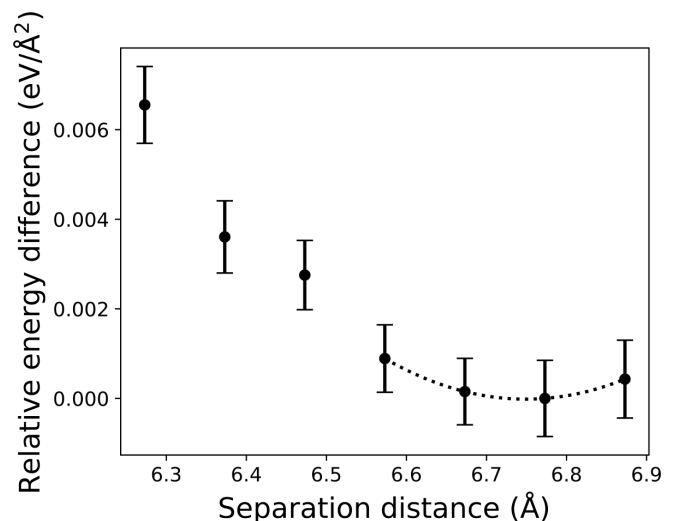


FIG. 6. FNDMC prediction of the binding curve of the monoclinic structure. The vertical axis indicates the relative energy differences from the lowest total energy. The dotted line indicates the quadratic fitting curve with the four lowest data points.
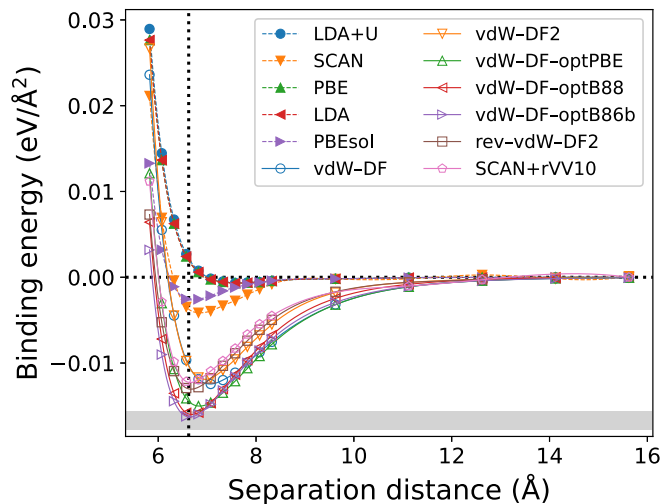
FIG. 7. DFT prediction of the interlayer binding curves of the monoclinic structure with different functionals. The experimental separation distance is shown as a vertical line. The binding energy predicted by FNDMC is shown as a gray shaded region. The PBE result is just behind the LDA result so the PBE curve is not visible.

shaded region indicates the interlayer binding energy predicted by FNDMC. The vertical width of the region indicates the error bar. The functionals without vdW corrections (i.e., LDA, PBE, LDA+$U$, PBEsol, and SCAN) completely fail to reproduce the interlayer binding. For vdW-corrected functionals, we estimated the minima (i.e., separation distance) by cubic spline interpolation. The predicted separation distances are shown in Table I with the experimental value [15].

Before discussing the results, we will briefly introduce vdW-corrected functionals, which are expressed as

$$E_{XC} = E_X^{GGA} + E_C^{LDA} + E_C^{NL}. \qquad (1)$$

Here, $E_X^{GGA}$ is the exchange functional, $E_C^{LDA}$ is the correlation functional of LDA, and $E_C^{NL}$ is the nonlocal correlation functional. $E_C^{NL}$ is given as

$$E_C^{NL} = \frac{1}{2} \iint d\vec{r} d\vec{r}' n(\vec{r}) \phi(\vec{r}, \vec{r}') n(\vec{r}'). \qquad (2)$$

TABLE I. Separation distances ($d_{\text{separation}}$) and binding energies ($E_{\text{binding}}$) of the monoclinic bulk CrI$_3$ obtained with different approaches. The top and bottom items are reference data.

| | $d_{\text{separation}}$ (Å) | $E_{\text{binding}}$ (meV/Å$^2$) |
|---|---|---|
| Experiment [15] | 6.623 | |
| FNDMC | 6.749(73) | 15.6–18.1 |
| vdW–DF | 7.063 | 12.45 |
| vdW–DF2 | 6.960 | 11.90 |
| rev–vdW–DF2 | 6.671 | 13.05 |
| SCAN+rVV10 | 6.656 | 12.27 |
| vdW–DF–optPBE | 6.847 | 15.02 |
| vdW–DF–optB88 | 6.686 | 15.99 |
| vdW–DF–optB86b | 6.646 | 16.30 |
| vdW–DF–optB86b [15] | 6.240 | |

Here, $n(\vec{r})$ is the electronic density at position $\vec{r}$. The term $\phi(\vec{r}, \vec{r}')$ is defined in Ref. [49] and determines the interaction among the densities. The term $E_{X-}^{GGA}$ is the revPBE exchange functional [56] in the original vdW–DF functional. The vdW–DF2 variant replaces the revPBE exchange functional with a revised PW86 exchange functional [57], because revPBE is generally too repulsive near the equilibrium separation [51]. rev-vdW–DF2 uses the B86b [58] exchange functional rather than PW86. This functional is designed to provide improved descriptions of inhomogeneous systems compared with PW86. For vdW–DF–optPBE, vdW–DF–optB88, and vdW–DF–optB86b functionals, the parameters in the exchange functionals, revPBE, B88 [59], and B86b [58], are optimized for the S22 data set to work with the vdW–DF correction [30]. SCAN+rVV10 combines the SCAN functional [48] and rVV10 correction for vdW interactions [60], which is similar to vdW–DF correction.

In Table I, as expected from previous experience, the vdW–DF functional overestimates the separation distance. The vdW–DF2 functional predicts a shorter distance, but the separation distance is still significantly larger than the experimental value. Similar overestimations have been reported in cases of transition metal atom adsorption on a graphene surface [17,18], interlayer binding of quasi–two-dimensional materials [18], and benzene adsorption on a copper surface [18]. On the other hand, rev–vdW–DF2 was found to be in extremely good agreement with the experimental value, presumably because it provides a better description of inhomogeneity through the use of the PW86b exchange functional. However, similar to vdW–DF and vdW–DF2, the rev–vdW–DF2 functional still significantly underestimates the binding energy. SCAN-rVV10 provides a similar prediction to that of rev–vdW–DF2. The functionals whose exchange portions were reoptimized with the vdW corrections (i.e., vdW–DF–optPBE, vdW–DF–optB88, and vdW–DF–optB86b) best reproduced the reference interlayer separation and binding energy. Among those functionals, vdW–DF–optPBE slightly overestimates the separation distance and underestimates the binding energy, presumably because the original revPBE functional generally overestimates interlayer repulsion. Finally, we note that our vdW–DF–opB86b results contradict a previous study: The estimation by McGuire *et al.* [15] of the separation distance, shown in the bottom column of Table I, significantly underestimates the separation distance compared with the experimental value.

The comparison between our results for CrI$_3$ and other benchmark studies of other quasi–two-dimensional materials shows that the best density functional is system dependent. Krogel *et al.* [20] predicted the equilibrium separation and the binding energy of TiS$_2$. They established that vdW–DF–optB86b and vdW–DF–optB88 reproduce both the reference equilibrium separation and binding energy. They also established that SCAN+rVV10 significantly underestimates the binding energy. Hamada [18] predicted the equilibrium separation of graphite, hexagonal boron nitride, and molybdenum (IV) sulfide with the vdW–DF2 and rev–vdW–DF2 functionals. Their findings suggest that vdW–DF2 significantly overestimates separation distances. On the other hand, their findings differ from our results in that, in the case of graphite,

vdW–DF2 reproduces the reference binding energy but rev–vdW–DF2 overestimates it. In the case of black phosphorus, vdW–DF–optB86b significantly overestimates the binding energy compared with the FNDMC prediction [19]. Schulz and Liljeroth [61] predicted the distances between atoms in hexagonal boron nitride (graphene) and Iridium (111) substrate. They showed that vdW–DF–optB88 reproduced the experimental structure for graphene but the functional underestimated the layer width in the case of the hexagonal boron nitride. They established that vdW–DF–rB86 [18,61], vdW–DF2–rB86 [18,61], and PBE+rVV10 [46,60] reproduced the experimental structures for both systems. However, their prediction heavily depends on the functional, suggesting that their results may not apply to other systems. Tran *et al.* [62] performed benchmark study of DFT functionals for intralayer and interlayer lattice constants and interlayer binding energy of several hexagonal layered solids. They established that PBE+rVV10L [63], SCAN+rVV10, and rev–vdW–DF2 showed comprehensively better performance than the other functionals including vdW–DF–optB86b and vdW–DF–optB88. To summarize, the accuracy of each DFT functional is significantly dependent on the target quasi–two-dimensional system: thus, functionals should be benchmarked for each system. Therefore, our study is a valuable source for subsequent DFT studies targeting $CrI_3$. We have found that some DFT functionals work impressively well for magnetic quasi–two-dimensional systems, for which DFT functionals have not been benchmarked against FNDMC to our knowledge. In addition, the reliable predictions of the binding energy of two-dimensional materials with FNDMC will be useful in further developing and improving DFT approximations.

## IV. CONCLUSIONS

In summary, we studied the interlayer binding properties of bulk $CrI_3$ using FNDMC. This method successfully reproduced the experimental interlayer separation distance [15] indicating the reliability of FNDMC for investigating bulk $CrI_3$. We also predicted the interlayer binding energy with FNDMC, which is estimated at 14.3 to 17.9 meV/Å$^2$. We found that, in agreement with experiment, the rhombohedral and monoclinic structures observed experimentally were within thermal energy difference, suggesting favorable cancellation of systematic errors in FNDMC. In this paper, we have carefully taken into account the different dimensional two-body finite-size errors of monolayer and monoclinic bulk $CrI_3$. We have evaluated several DFT functionals based on the predicted binding energy and the experimental interlayer separation distance. The results showed that functionals with vdW corrections, vdW–DF–optB88, and vdW–DF–optB86b reproduced the reference interlayer separation distance and binding energies very well. We believe that the FNDMC predicted interlayer binding energy is useful to test other promising functionals such as vdW-DF-C09 [64], vdW-DF-cx [65], DFT-D [66–68], TS-vdW [69], and ones not yet invented, in future. Especially, vdW-DF-cx was shown as good as vdW-DF-B86b in a previous benchmark study [70].

## APPENDIX

### 1. Energy difference of the rhombohedral and monoclinic structures

We calculated the energy differences of the rhombohedral and monoclinic structures with FNDMC. The structures compared have the same experimental geometries considered in the main text [15]. The energies were calculated for the ferromagnetic state with 3 bohr/f.u.. We compared the energies of simulation cells with the same number of atoms and a similar shape for both structures (three layers and 12 f.u. in total), so that the two-body finite-size errors could be canceled out in the energy difference prediction; however, the residual finite-size errors were shown to be large without extrapolation.

The energy difference of the two structural phases was considered to be a few meV per atom, since the transition temperatures were below the room temperature. Our FNDMC calculations found a 90(28) meV/f.u. energy difference, without finite-size correction. This result, although encouraging, may well be due to accidental cancellation of multiple errors sources, since, in addition to size effects, nodal errors and nonlocality pseudopotential errors were typically much larger than a few meV per atom. Finite-size extrapolations using FNDMC are currently not practical for the rhombohedral structure.

### 2. DFT predicted binding curves of the rhombohedral structure

In Fig. 8, we compare the interlayer binding curves predicted by DFT with different functionals. Since the energy difference between the monoclinic and rhombohedral structure is very small, the binding energy should be close. Therefore we write the FNDMC prediction of the binding energy for the monoclinic structure into the figure as the reference for the binding energy. We obtained very similar results to those for the monoclinic structure.
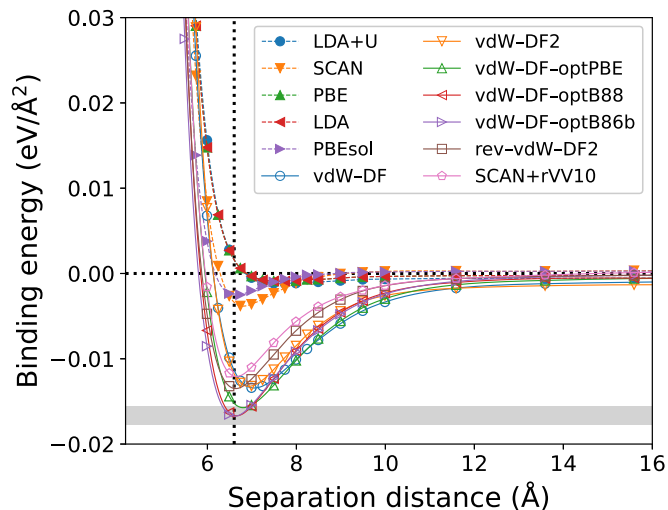


FIG. 8. DFT prediction of the interlayer binding curves of the rhombohedral structure with different functionals. The experimental separation distance is shown as a vertical line. The binding energy predicted by FNDMC is shown as a gray shaded region. The PBE result is just behind the LDA result so the PBE curve is not visible.

[1] G. Fiori, F. Bonaccorso, G. Iannaccone, T. Palacios, D. Neumaier, A. Seabaugh, S. K. Banerjee, and L. Colombo, Nat. Nanotechnol. **9**, 768 (2014).

[2] G. R. Bhimanapati, Z. Lin, V. Meunier, Y. Jung, J. Cha, S. Das, D. Xiao, Y. Son, M. S. Strano, V. R. Cooper *et al.*, ACS Nano **9**, 11509 (2015).

[3] F. Xia, H. Wang, D. Xiao, M. Dubey, and A. Ramasubramaniam, Nat. Photonics **8**, 899 (2014).

[4] M. Xu, T. Liang, M. Shi, and H. Chen, Chem. Rev. **113**, 3766 (2013).

[5] S. Z. Butler, S. M. Hollen, L. Cao, Y. Cui, J. A. Gupta, H. R. Gutiérrez, T. F. Heinz, S. S. Hong, J. Huang, A. F. Ismach *et al.*, ACS Nano **7**, 2898 (2013).

[6] B. Huang, G. Clark, E. Navarro-Moratalla, D. R. Klein, R. Cheng, K. L. Seyler, D. Zhong, E. Schmidgall, M. A. McGuire, D. H. Cobden *et al.*, Nature **546**, 270 (2017).

[7] C. Gong, L. Li, Z. Li, H. Ji, A. Stern, Y. Xia, T. Cao, W. Bao, C. Wang, Y. Wang *et al.*, Nature **546**, 265 (2017).

[8] J. L. Lado and J. Fernández-Rossier, 2D Mater. **4**, 035002 (2017).

[9] V. K. Gudelli and G.-Y. Guo, New J. Phys. **21**, 053012 (2019).

[10] The magnetic state of the trilayer CrI$_3$ has been denoted as ferromagnetic, antiferromagnetic, or ferrimagnetic [6,9,14]. We denote it here as ferrimagnet.

[11] T. Song, X. Cai, M. W.-Y. Tu, X. Zhang, B. Huang, N. P. Wilson, K. L. Seyler, L. Zhu, T. Taniguchi, K. Watanabe *et al.*, Science **360**, 1214 (2018).

[12] D. R. Klein, D. MacNeill, J. L. Lado, D. Soriano, E. Navarro-Moratalla, K. Watanabe, T. Taniguchi, S. Manni, P. Canfield, J. Fernández-Rossier, and P. Jarillo-Herrero, Science **360**, 1218 (2018).

[13] B. Huang, G. Clark, D. R. Klein, D. MacNeill, E. Navarro-Moratalla, K. L. Seyler, N. Wilson, M. A. McGuire, D. H. Cobden, D. Xiao *et al.*, Nat. Nanotechnol. **13**, 544 (2018).

[14] T. Song, Z. Fei, M. Yankowitz, Z. Lin, Q. Jiang, K. Hwangbo, Q. Zhang, B. Sun, T. Taniguchi, K. Watanabe *et al.*, Nat. Mater. **18**, 1298 (2019).

[15] M. A. McGuire, H. Dixit, V. R. Cooper, and B. C. Sales, Chem. Mater. **27**, 612 (2015).

[16] N. Sivadas, S. Okamoto, X. Xu, C. J. Fennie, and D. Xiao, Nano Lett. **18**, 7658 (2018).

[17] I. Lončarić and V. Despoja, Phys. Rev. B **90**, 075414 (2014).

[18] I. Hamada, Phys. Rev. B **89**, 121103(R) (2014).

[19] L. Shulenburger, A. Baczewski, Z. Zhu, J. Guan, and D. Tománek, Nano Lett. **15**, 8170 (2015).

[20] J. T. Krogel, S. F. Yuk, P. R. C. Kent, and V. R. Cooper, J. Phys. Chem. A **124**, 9867 (2020).

[21] W. M. Foulkes, L. Mitas, R. J. Needs, and G. Rajagopal, Rev. Mod. Phys. **73**, 33 (2001).

[22] H. Shin, J. Kim, H. Lee, O. Heinonen, A. Benali, and Y. Kwon, J. Chem. Theory Comput. **13**, 5639 (2017).

[23] E. Mostaani, N. D. Drummond, and V. I. Fal'ko, Phys. Rev. Lett. **115**, 115501 (2015).

[24] S. Azadi and T. D. Kühne, Phys. Rev. B **97**, 205428 (2018).

[25] P. Ganesh, J. Kim, C. Park, M. Yoon, F. A. Reboredo, and P. R. C. Kent, J. Chem. Theory Comput. **10**, 5318 (2014).

[26] C.-R. Hsing, C. Cheng, J.-P. Chou, C.-M. Chang, and C.-M. Wei, New J. Phys. **16**, 113015 (2014).

[27] J. Ahn, I. Hong, G. Lee, H. Shin, A. Benali, and Y. Kwon, J. Phys. Chem. C **124**, 24420 (2020).

[28] D. Wines, K. Saritas, and C. Ataca, J. Chem. Phys. **153**, 154704 (2020).

[29] Y. Kadioglu, J. A. Santana, H. D. Özaydin, F. Ersan, O. Ü. Aktürk, E. Aktürk, and F. A. Reboredo, J. Chem. Phys. **148**, 214706 (2018).

[30] J. Klimeš, D. R. Bowler, and A. Michaelides, J. Phys.: Condens. Matter **22**, 022201 (2009).

[31] J. Kim, A. D. Baczewski, T. D. Beaudet, A. Benali, M. C. Bennett, M. A. Berrill, N. S. Blunt, E. J. L. Borda, M. Casula, D. M. Ceperley *et al.*, J. Phys.: Condens. Matter **30**, 195901 (2018).

[32] P. Giannozzi, S. Baroni, N. Bonini, M. Calandra, R. Car, C. Cavazzoni, D. Ceresoli, G. L. Chiarotti, M. Cococcioni, I. Dabo *et al.*, J. Phys.: Condens. Matter **21**, 395502 (2009).

[33] M. Burkatzki, C. Filippi, and M. Dolg, J. Chem. Phys. **126**, 234105 (2007).

[34] M. Burkatzki, C. Filippi, and M. Dolg, J. Chem. Phys. **129**, 164115 (2008).

[35] A. L. Dzubak, T. Ichibha, J. T. Krogel, V. R. Cooper, and F. A. Reboredo, Diffusion quantum monte carlo study of halogen and chromium-halogen complexes, (2020), unpublished.

[36] J. T. Krogel, J. A. Santana, and F. A. Reboredo, Phys. Rev. B **93**, 075143 (2016).

[37] C. J. Umrigar, J. Toulouse, C. Filippi, S. Sorella, and R. G. Hennig, Phys. Rev. Lett. **98**, 110201 (2007).

[38] N. D. Drummond, R. J. Needs, A. Sorouri, and W. M. C. Foulkes, Phys. Rev. B **78**, 125106 (2008).

[39] P. P. Ewald, Ann. Phys. **369**, 253 (1921).

[40] QMCPACK, User's Guide and Developer's Manual v3.9.2, online: https://docs.qmcpack.org/qmcpack_manual_v3.9.2.pdf (2020), accessed on 16Nov2020.

[41] QMCPACK Google group, strange results when changing lattice parameters, online: https://groups.google.com/g/qmcpack/c/3Hkt5sWY_e4/m/6P8aUWGaAQAJ (2020), accessed on 19Nov2020.

[42] J. T. Krogel, Comput. Phys. Commun. **198**, 154 (2016).

[43] G. Kresse and J. Furthmüller, Comput. Mater. Sci. **6**, 15 (1996).

[44] G. Kresse and D. Joubert, Phys. Rev. B **59**, 1758 (1999).

[45] D. M. Ceperley and B. J. Alder, Phys. Rev. Lett. **45**, 566 (1980).

[46] J. P. Perdew, K. Burke, and M. Ernzerhof, Phys. Rev. Lett. **77**, 3865 (1996).

[47] G. I. Csonka, J. P. Perdew, A. Ruzsinszky, P. H. T. Philipsen, S. Lebègue, J. Paier, O. A. Vydrov, and J. G. Ángyán, Phys. Rev. B **79**, 155107 (2009).

[48] J. Sun, A. Ruzsinszky, and J. P. Perdew, Phys. Rev. Lett. **115**, 036402 (2015).

[49] M. Dion, H. Rydberg, E. Schröder, D. C. Langreth, and B. I. Lundqvist, Phys. Rev. Lett. **92**, 246401 (2004).

[50] G. Román-Pérez and J. M. Soler, Phys. Rev. Lett. **103**, 096102 (2009).

[51] K. Lee, E. D. Murray, L. Kong, B. I. Lundqvist, and D. C. Langreth, Phys. Rev. B **82**, 081101(R) (2010).

[52] H. Peng, Z.-H. Yang, J. P. Perdew, and J. Sun, Phys. Rev. X **6**, 041005 (2016).

[53] S. L. Dudarev, G. A. Botton, S. Y. Savrasov, C. J. Humphreys, and A. P. Sutton, Phys. Rev. B **57**, 1505 (1998).

[54] T. Thonhauser, S. Zuluaga, C. A. Arter, K. Berland, E. Schröder, and P. Hyldgaard, Phys. Rev. Lett. **115**, 136402 (2015).

[55] See Supplemental Material at http://link.aps.org/supplemental/10.1103/PhysRevMaterials.5.064006 reference here.

[56] Y. Zhang and W. Yang, Phys. Rev. Lett. **80**, 890 (1998).

[57] J. P. Perdew and Y. Wang, Phys. Rev. B **33**, 8800 (1986).

[58] A. D. Becke, J. Chem. Phys. **85**, 7184 (1986).

[59] A. D. Becke, Phys. Rev. A **38**, 3098 (1988).

[60] R. Sabatini, T. Gorni, and S. de Gironcoli, Phys. Rev. B **87**, 041108(R) (2013).

[61] F. Schulz, P. Liljeroth, and A. P. Seitsonen, Phys. Rev. Materials **3**, 084001 (2019).

[62] F. Tran, L. Kalantari, B. Traoré, X. Rocquefelte, and P. Blaha, Phys. Rev. Materials **3**, 063602 (2019).

[63] H. Peng and J. P. Perdew, Phys. Rev. B **95**, 081105(R) (2017).

[64] V. R. Cooper, Phys. Rev. B **81**, 161104(R) (2010).

[65] K. Berland and P. Hyldgaard, Phys. Rev. B **89**, 035412 (2014).

[66] S. Grimme, J. Comput. Chem. **25**, 1463 (2004).

[67] S. Grimme, J. Comput. Chem. **27**, 1787 (2006).

[68] S. Grimme, J. Antony, S. Ehrlich, and H. Krieg, J. Chem. Phys. **132**, 154104 (2010).

[69] A. Tkatchenko and M. Scheffler, Phys. Rev. Lett. **102**, 073005 (2009).

[70] T. Björkman, J. Chem. Phys. **141**, 074708 (2014).

[71] http://energy.gov/downloads/doe-public-access-plan.